

## Sintering of nickel steam-reforming catalysts: effects of temperature and steam and hydrogen pressures

Jens Sehested,<sup>a,\*</sup> Johannes A.P. Gelten,<sup>a,1</sup> Ioannis N. Remediakis,<sup>b</sup>  
Hanne Bengaard,<sup>b</sup> and Jens K. Nørskov<sup>b</sup>

<sup>a</sup> Haldor Topsøe A/S, Nymøllevej 55, DK-2800, Denmark

<sup>b</sup> Center for Atomic-scale Materials Physics, and Interdisciplinary Research Center for Catalysis, Department of Physics,  
Technical University of Denmark, DK-2800 Lyngby, Denmark

Received 20 November 2003; revised 21 January 2004; accepted 25 January 2004

### Abstract

Steam reforming over nickel catalysts is widely used for industrial-scale production of hydrogen and synthesis gas. This work is a study of the effects of atmosphere and temperature on the rate of sintering of nickel steam-reforming catalysts. The relative nickel areas of Ni/MgAl<sub>2</sub>O<sub>4</sub> and Ni/Al<sub>2</sub>O<sub>3</sub> catalysts after sintering in H<sub>2</sub>O:H<sub>2</sub> atmospheres at high (40 bar) and low (1 bar) pressures are reported. The data are discussed in terms of the recently proposed model for the sintering rate of supported nickel catalysts [J. Sehested, *J. Catal.* 217 (2003) 417] and density functional theory (DFT) calculations of the stability and diffusivity of transport species at the surface of nickel particles. OH-bonded nickel dimers are found to have a much lower energy of formation than nickel adatoms ( $\Delta E = 58 \text{ kJ mol}^{-1}$ ). It is therefore concluded that in steam/hydrogen mixtures, OH-bonded nickel dimers are dominating the surface transport on nickel particles and consequently sintering via particle migration and coalescence. Expressions connecting the diffusion constant for nickel particles to the diffusion constant and energy of formation of nickel adatoms and of OH-bonded nickel dimers are given. These equations are used in a sintering model [J. Sehested, *J. Catal.* 217 (2003) 417] and good agreement between the model and the experimental data is obtained at moderate temperatures. Above temperatures of ca. 600 °C at 40 bar and approximately 700 °C at 1 bar total pressure, the rate and the activation energy of sintering increase considerably. The reason for this observation may be that sintering via Ostwald ripening dominates the sintering rate under these conditions.

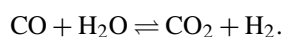
© 2004 Published by Elsevier Inc.

**Keywords:** Steam reforming; Nickel catalyst; Sintering; DFT calculations; Particle migration

### 1. Introduction

Sintering of heterogeneous catalysts is often referred to as the loss of catalytic surface area due to growth of large particles at the expense of smaller particles. Sintering is complex and may be influenced by many parameters such as sintering time, temperature, chemical environment, catalyst composition and structure, and support morphology. A good understanding of the sintering mechanism is necessary, both to predict the extent of deactivation by sintering and to design catalysts that maintain a high activity.

Sintering is the reason for loss of activity for many industrial catalyst systems. An industrial process, where sintering is important, is steam reforming over supported nickel catalysts:



Modern steam-reforming units consist of a primary reformer with an adiabatic prereformer upstream, which reduces the load of the primary reformer, and minimizes the risk of sulfur poisoning [1,2]. Both the prereformer and the primary reformer are operated at 30 bar total pressure and high pressures of steam corresponding to an oxygen to carbon ratio of approximately 2–4. The temperatures are in the range 400–550 and 500–950 °C, respectively. In both the pri-

\* Corresponding author. Fax: +45 45272999.

E-mail address: [JSS@topsoe.dk](mailto:JSS@topsoe.dk) (J. Sehested).

<sup>1</sup> Department of Chemical Engineering, University of Twente, Postbus 217, 7500 AE Enschede, Netherlands.

mary reformer and the prereformer, Ni-based catalysts are commonly used [1,2].

Nickel steam-reforming catalysts are subject to several deactivation mechanisms including coking, poisoning, and sintering. Particle growth via sintering influences the resistance of the catalyst toward coking and poisoning with sulfur. The coking limits are affected by the nickel particle size and the nickel surface area determines the sulfur capacity of the catalyst [1,2]. Furthermore, the activity of a steam-reforming catalyst is related to the nickel surface area. To model an industrial reformer with regard to activity and the effect of sulfur poisoning, it is necessary to know the nickel surface area as a function of time, temperature, feed gas composition, chemical composition including promoters, and extent of poisoning.

Several studies of sintering of Ni particles supported on a ceramic carrier are reported in the literature [1–12]. The most important parameters are the sintering temperature and the composition of the gas over the catalyst [7]. Increasing temperature and the presence of steam accelerates the sintering process [7]. High surface areas of the carrier, on the other hand, increase the stability toward sintering [3,8–10,13–15].

Three mechanisms for the metal particle growth have been proposed: (i) particle migration, where entire crystallites migrate over the support followed by coalescence; (ii) Ostwald ripening (atom migration), where metal atoms emitted from one crystallite migrate over the support and are captured by another crystallite; and (iii) vapor transport between particles (at high temperatures).

Sehested et al. [8] studied the mechanism for sintering of nickel steam-reforming catalysts at 500 °C, 30 bar, H<sub>2</sub>O:H<sub>2</sub> = 10:1 and concluded on the basis of the particle size distributions that sintering occurred via the crystallite migration mechanism. For this sintering mechanism mass transport by diffusion of nickel atoms on the nickel crystallite surfaces is necessarily an important step, so the diffusivity and concentration of single metal atoms and small clusters are central parameters in the understanding of the sintering phenomenon.

Campbell et al. [16] reported that the heat of adsorption of metal atoms to metal particles depends more strongly on the particle size than assumed previously leading to faster rates of sintering via both Ostwald ripening and particle migration and coalescence. This phenomenon is most important for small particles (diameter < 50 Å for Pb particles). A nickel particle with a diameter of approximately 36 Å contains the same number of atoms as a Pb particle with a diameter of 50 Å due to the size difference of the atoms. In the present study, the nickel particles are generally larger than this particle size. The smallest average nickel particle diameters estimated from the nickel surface areas in the catalysts used here are of the order of 75–90 Å [11], indicating that the effect of fast sintering of small particles can be ignored. Contrary, ASAXS (anomalous small angle X-ray scattering) gives lower estimates of the nickel particle diameters [11], indicating that sintering of small particles is significant.

However, we believe that the measurements of the nickel areas in this case give the most reliable estimates of the nickel particle diameters as these measurements are carried out using reduced catalysts as opposed to ASAXS, where passivated catalysts are used. Nickel may move significantly during passivation. For this reason and for simplicity, we have chosen to neglect the effects observed by Campbell et al. [16] in the following.

Recently, a simple expression for the development of the nickel surface area as a function of time, temperature, nickel loading, and carrier surface area was derived [9]. To obtain the expression it was assumed that the sintering mechanism was particle migration and coalescence, that the particle sizes were log normally distributed with constant relative standard deviation, and that the carrier acted only as an area dispersing the metal particles. The expression included a parameter, which depends on the atmosphere over the catalyst and the chemical environment on the catalyst.

The objective of the present work is to investigate experimentally and theoretically the effects of steam and hydrogen over nickel catalysts as a function of temperature. The relative nickel areas of Al<sub>2</sub>O<sub>3</sub> and MgAl<sub>2</sub>O<sub>4</sub>-supported nickel catalysts are determined after sintering at 1, 31, and 40 bar total pressure at various steam and hydrogen ratios and compared to previously published data. The experimentally observed effects of steam and hydrogen pressures are rationalized theoretically using density functional theory (DFT) calculations and the sintering model published recently [9].

## 2. Experimental

Three supported nickel catalysts were studied. The first catalyst (catalyst No. 1) contained 22 wt% nickel and was supported on a 24 m<sup>2</sup> g<sup>-1</sup> MgAl<sub>2</sub>O<sub>4</sub> carrier. Catalyst No. 2 contained 9.5 wt% nickel and was supported on a high surface area (144 m<sup>2</sup> g<sup>-1</sup>)  $\theta$ - and  $\eta$ -Al<sub>2</sub>O<sub>3</sub> support. The last catalyst (catalyst No. 3) was prepared using a 121 m<sup>2</sup> g<sup>-1</sup>  $\theta$ - and  $\eta$ -Al<sub>2</sub>O<sub>3</sub> and had 19.4 wt% nickel. The catalysts were reduced in hydrogen at 525 °C for 4 h and passivated overnight at 25–50 °C in a mixture of 1 v/v% air in N<sub>2</sub> followed by 2 h in 5 v/v% air in N<sub>2</sub> before they were removed from the reactor. Prior to sintering, the catalysts were reactivated by reduction in H<sub>2</sub> at 500 °C for 2 h.

Sintering experiments were performed at both high and low pressures and the detailed sintering conditions are given in Table 1. In the first set of sintering experiments, samples of catalyst No. 1 were exposed to a 2.5:1 mixture of steam and hydrogen at 484–692 °C and a total pressure of 40 bar. The experiments were performed with a temperature gradient over the reactor. The temperature of each sample was obtained by temperature measurements at the position of the catalyst sample as discussed further below. In the second set of experiments, catalyst No. 2 was sintered at ambient pressure, H<sub>2</sub>O:H<sub>2</sub> = 1:1, and at temperatures in the range 500–825 °C. Separate experiments were performed for each

Table 1  
Sintering conditions

Series No.	Catalyst No.	$P_{\text{H}_2\text{O}}/P_{\text{H}_2}$	Total pressure (bar)	Temperatures (°C)	Time (h)
1	1 (22% Ni/MgAl <sub>2</sub> O <sub>4</sub> )	2.5	40	483–682	700
2	2 (9.5% Ni/Al <sub>2</sub> O <sub>3</sub> )	1 10	1 31	500–825 500	50 115
3	3 (19.4% Ni/Al <sub>2</sub> O <sub>3</sub> )	0.2–25	1	550	50

temperature. Catalyst No. 2 was also sintered for 115 h at 31 bar total pressure and  $\text{H}_2\text{O}:\text{H}_2 = 10:1$ . Finally, a third series of experiments was conducted using catalyst No. 3 at 1 bar total pressure of  $\text{H}_2$ ,  $\text{H}_2\text{O}$ , and  $\text{N}_2$ , and a temperature of 550 °C with the  $\text{H}_2\text{O}:\text{H}_2$  ratio varied in the range 0.2–25.

The experimental setup used for these experiments was operated at a total pressure of 1 to 40 bar and at high pressures of steam. All parts of the system, where high partial pressures of steam were present, could be heated. The temperature of the gas at the top of the catalyst bed was controlled by a thermocouple on the outside wall of a steel reactor and the actual temperature in the bed was measured by a movable thermocouple in a small tube through the center of the reactor. The catalysts were kept at the bottom of small stainless-steel nets, which fitted in the reactor and over the internal tube. The bottom of the nets covered the cross section of the reactor. The length of the part of the reactor containing nets was 25–30 cm.

The surface areas (BET) of selected catalyst samples were determined by nitrogen adsorption using a Quantachrome MONOSORB apparatus. The measured values were normalized to standard temperature and pressure in accordance with the ASTM standard for single-point determination of BET surface areas [17]. The surface area of the internal standard was measured daily giving a standard deviation of less than 2%.

X-ray powder diffraction (XRD) was used to determine the phase composition of the fresh catalysts. The XRD measurements were performed on a Philips PW1820 goniometer with Bragg–Bretano geometry, a variable divergence slit and a graphite monochromator using  $\text{Cu-K}\alpha$  radiation.

The sulfur chemisorption capacity was used to determine the nickel surface area relative to that of the fresh catalysts. The relative nickel surface area,  $A_{\text{Ni}}$ , is converted to a relative surface-averaged nickel particle diameter,  $\bar{d}_s$ , by the following expression,

$$\bar{d}_s = \text{const} \frac{X_{\text{Ni}}}{A_{\text{Ni}}}, \quad (1)$$

where  $X_{\text{Ni}}$  is the fractional nickel loading (Ni wt%/100). Chemisorption of sulfur was carried out in a separate reactor according to Rostrup-Nielsen and co-workers [1,2] using a mixture of  $\text{H}_2\text{S}/\text{H}_2$  until saturation. Under these experimental conditions, the Ni surface area is proportional to the sulfur capacity. The sulfur uptake of a catalyst was determined

by oxidation of chemisorbed sulfur at high temperatures and the amount of liberated  $\text{SO}_2$  was measured by infrared detection. The chemisorption of sulfur is discussed in more detail by Alstrup et al. [18].

The nickel surface areas obtained by sulfur chemisorption have been compared to those determined by hydrogen chemisorption [2] and anomalous small angle X-ray scattering [11]. In these studies it was found that nickel surface areas determined by sulfur chemisorption are proportional to those obtained by hydrogen chemisorption and ASAXS. However, the conversion factors for converting nickel areas measured by sulfur chemisorption to nickel areas acquired by hydrogen chemisorption and ASAXS were not the same. Only nickel surface areas and nickel particle diameters relative to those of the fresh samples are used in the following.

### 3. Computational details

The calculations were carried out using self-consistent density functional theory. The DACAPO package [19] was employed.

The ionic cores and their interaction with valence electrons are described by ultrasoft pseudopotentials [20]. Exchange and correlation effects are taken into account via the generalized gradient approximation (GGA) and the revised Perdew–Burke–Ernzerhof (RPBE) functional [21]. The wave function was expanded in a plane-wave basis with a kinetic energy cutoff of 25 Ry. The valence electron density is obtained by self-consistent iterative diagonalization of the Hamiltonian [22], with Pulay mixing of the output and input densities. Occupation of the one-electron states was calculated using a temperature of  $k_{\text{B}}T = 19 \text{ kJ mol}^{-1}$  (0.2 eV); all energies have been extrapolated to  $T = 0$ . The ionic degrees of freedom were relaxed using a conjugate-gradient minimization, until the maximum force component was smaller than  $5 \text{ kJ mol}^{-1} \text{ \AA}^{-1}$  (0.05 eV  $\text{\AA}^{-1}$ ). We considered spin-polarized electron densities, in order to take into account the magnetic moment of Ni atoms.

We use the periodic slab approximation. Our unit cell contains three layers of Ni parallel to the (111) plane, separated by about 11 Å of vacuum. A slab thickness of three layers is the minimum thickness required in order to distinguish between fcc and hcp hollow sites on Ni(111). Increase of the slab thickness beyond 3 layers seems to result in very small changes in adsorption and activation energies of various molecules on Ni(111) (see, for example, Ref. [23]). We used a  $(2 \times 2)$  supercell for the calculations of Ni adatoms. For the calculations regarding the  $\text{Ni}_2\text{-OH}$  complex, we used a  $(3 \times 3)$  unit cell. In all cases, the supercell was chosen so that the minimum distance between an adsorbate atom and its periodic image is at least 5 Å, roughly twice the Ni–Ni distance in bulk Ni. All adsorbates were fully allowed to relax. Allowing the topmost Ni atoms of the simulation slab to relax did not result in any significant displacement for the case of a Ni adatom. Therefore we kept all Ni atoms in the

slab fixed for the rest of the calculations. The Brillouin zone of the system was modeled by 9 and 6 special  $\mathbf{k}$  points of the Chadi–Cohen type [24] for the  $(2 \times 2)$  and  $(3 \times 3)$  unit cells, respectively. We use a dipole correction in the vacuum region, to account for the dipole moment of OH on the top side of the slab.

The location of transition states and the calculation of energy barriers are performed using the Nudged Elastic Band method [25]. In all cases, we used five configurations along the path (initial and final states and three intermediate configurations). The path was relaxed, until the change in energy barrier was smaller than  $0.5 \text{ kJ mol}^{-1}$ .

#### 4. Experimental results

In this section, the results obtained in the three sets of sintering experiments are described. In the first set of experiments the temperature dependence of the relative nickel surface area was studied at high pressure (40 bar). Seven samples of catalyst No. 1 (22 wt% Ni/MgAl<sub>2</sub>O<sub>4</sub>) were placed at different positions from the top to the bottom of the reactor and heated in 40 bar of N<sub>2</sub> to a temperature of about 400 °C at the entrance and about 650 °C at the exit of the catalyst bed. After the temperature was stabilized, hydrogen and then steam were allowed into the reactor such that a H<sub>2</sub>O:H<sub>2</sub> ratio of 2.5:1 was obtained and the flow of nitrogen was switched off. The temperature was then increased to reach the desired temperature range of 450–700 °C. The temperature at the position of each catalyst sample was carefully measured using the movable thermocouple inside the internal tube in the reactor. These conditions were kept constant for 700 h. After shutdown, the relative nickel surface areas of the catalyst samples were determined by sulfur chemisorption.

The data are plotted in Fig. 1 as a function of the temperature at the position of the catalyst sample,  $T$  (°C). The relative nickel surface areas reported recently by Sehested [9] after sintering of the same type of catalyst at 31 bar and H<sub>2</sub>O:H<sub>2</sub> = 10:1 for 700 h are plotted in the figure for comparison. Both sets of data show that temperature is an important parameter for the rate of sintering. It is worth noting that the pressure of steam used for the two data sets plotted in Fig. 1 were very similar, 28.5 and 28.2 bar, for this work and that reported in the literature, respectively. However, the hydrogen pressure in the present experiment was four times that used by Sehested [9]. Interestingly, the effect of an increase in the hydrogen pressure is a decrease in the rate of sintering. This rather surprising effect of the hydrogen partial pressure is discussed in detail in a later section.

The first part of the second set of experiments consisted of five separate sintering experiments at ambient pressure using catalyst No. 2 (9.5 wt% Ni/Al<sub>2</sub>O<sub>3</sub>). In all five experiments the sintering time was 50 h and the H<sub>2</sub>O:H<sub>2</sub> ratio was 1. The second part of the second set of experiments consisted of a sintering treatment at 500 °C, 31 bar, and H<sub>2</sub>O:H<sub>2</sub> = 10:1 for 115 h. After shutdown of both types of

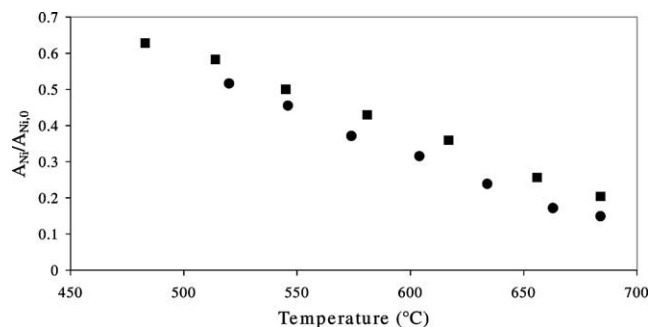


Fig. 1. The relative nickel surface areas of catalysts containing 22 wt% nickel supported on a MgAl<sub>2</sub>O<sub>4</sub> carrier (catalyst No. 1) plotted as a function of the measured temperature at the position of the catalyst sample. The catalysts were sintered for 700 h in atmospheres containing steam and hydrogen in a ratio of 2.5:1 and at 40 bar total pressure (filled squares, this work) or at a steam to hydrogen ratio of 10:1 and 31 bar total pressure (filled circles, [9]).

Table 2

Results of the second series of experiments using catalyst No. 2 (9.5 wt% Ni/Al<sub>2</sub>O<sub>3</sub>)

Temperature (°C)	HBET areas (m <sup>2</sup> g <sup>-1</sup> )	$P_{\text{H}_2\text{O}}/P_{\text{H}_2}$	Total pressure (bar)	$A_{\text{Ni}}/A_{\text{Ni},0}$	$d_{\text{Ni}}/d_{\text{Ni},0}$
500	122	1	1	0.855	1.17
575	113	1	1	0.699	1.43
650	105	1	1	0.585	1.71
750	95.8	1	1	0.309	3.24
825	84.8	1	1	0.244	4.10
500	98.5	10	31	0.474	2.11

The sintering times were 115 and 50 h at high and low pressures, respectively.

experiments, the relative nickel surface areas of the catalyst samples were determined by sulfur chemisorption. The data are given in Table 2. As seen from the table the temperature also has a pronounced effect on the nickel surface area of this catalyst. In addition, the effect of an elevated total pressure is a significant increase in the rate of sintering at 500 °C (111% increase in  $d_{\text{Ni}}/d_{\text{Ni},0}$  at 31 bar versus 17% at 1 bar). This point is examined in detail later in Section 7. As an increase in the partial pressure of hydrogen tends to slow down the sintering, an increased partial pressure of steam must increase the rate of sintering. These observations support the results of Bartholomew et al. [12] who showed that the loss of nickel surface area in a Ni/ $\delta$ -alumina catalyst is significantly faster in a 3% H<sub>2</sub>O/H<sub>2</sub> mixture than in a pure H<sub>2</sub> atmosphere.

Finally, the results from the third series of experiments, where catalyst No. 3 is sintered at 550 °C, atmospheric pressure, and with the  $P_{\text{H}_2\text{O}}/P_{\text{H}_2}$  ratio varied from 0.2 to 25, are presented. In all four experiments the sintering time was 50 h. After shutdown of the experiments, the relative nickel surface areas of the catalyst samples were determined by sulfur chemisorption and the results are given in Table 3. As seen from this table an increase in the  $P_{\text{H}_2\text{O}}/P_{\text{H}_2}$  ratio tends to increase the sintering rate. The discussion of this result

Table 3  
Results from the third series of experiments using catalyst No. 3

$P_{\text{H}_2\text{O}}$ (bar)	$P_{\text{H}_2}$ (bar)	$P_{\text{N}_2}$ (bar)	$P_{\text{H}_2\text{O}}/P_{\text{H}_2}$	$A_{\text{Ni}}/A_{\text{Ni},0}$	$d_{\text{Ni}}/d_{\text{Ni},0}$
0.067	0.333	0.6	0.2	0.78	1.28
0.33	0.33	0.33	1	0.68	1.47
0.5	0.063	0.437	8	0.69	1.44
0.5	0.02	0.48	25	0.61	1.65

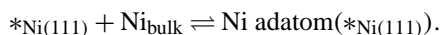
The sintering time was 50 h and the sintering conditions were 1 bar total pressure and 550 °C.

and a more quantitative interpretation of the data are given in the following sections.

## 5. Stability of transport species at nickel surfaces

In the particle migration and coalescence sintering mechanism, the diffusivity and the abundance of single metal atoms and small metal clusters on the metal surface are central parameters for the rate of sintering. The increased sintering rate due to adsorbed molecules was studied in detail for hydrogen on platinum by Horch et al. [26] and for sulfur at copper by Feibelman [27]. Horch et al. [26] concluded that a Pt–H complex on a Pt(110) surface has a strongly increased diffusivity relative to that of a Pt adatom; hence the rate of sintering of Pt is enhanced in hydrogen. Feibelman studied the energetics of diffusion of small copper islands at Cu(111) theoretically and showed that the energy of formation of a Cu adatom and a  $\text{Cu}_3\text{S}_3$  island are 77 and 27  $\text{kJ mol}^{-1}$ , respectively. The energy of diffusion for  $\text{Cu}_3\text{S}_3$  was 28  $\text{kJ mol}^{-1}$  higher than that for a Cu adatom. On this basis, Feibelman suggests that the experimentally observed enhancement in the rate of ripening of monolayer thick Cu islands at Cu(111) films in the presence of sulfur is due to an increase in the number of Cu-transport species.

The transport species at the surface of nickel crystallites may be single atoms or small clusters of nickel and both may be bonded to absorbing species. We will show here that on Ni(111) a nickel-dimer bonded to an OH radical is a very stable adspecies. When no external adsorbate is present, the lowest energy adspecies is a nickel adatom. A nickel adatom may be formed by emission of a nickel atom from a kink site at the nickel surface. Formation of an adatom by emission of an atom from a kink takes place with conservation of the number of edge and kink sites. Therefore the energy change in the reaction equals that of a nickel atom moved from the bulk of the nickel particle to the nickel surface as an adatom:



We have determined the energy cost of forming an adatom from a kink to be 112  $\text{kJ mol}^{-1}$ . The equilibrium constant for formation of a nickel adatom,  $K_1$ , and the coverage of nickel adatoms,  $\theta_{\text{add-atom}}$ , are given by

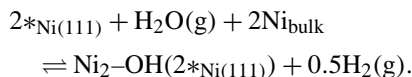
$$K_1 = \frac{\theta_{\text{add-atom}}}{1 - \theta_{\text{add-atom}}} \Leftrightarrow \theta_{\text{add-atom}} = \frac{K_1}{1 + K_1}. \quad (2)$$

Considering the high energy of formation of a nickel adatom, the coverage of nickel adatoms is assumed to be small and hence  $\theta_{\text{add-atom}}$  is given by

$$\theta_{\text{add-atom}} \approx K_1. \quad (3)$$

As discussed in the Introduction and observed in the section presenting the experimental results, high pressures of steam give rise to an increased rate of sintering while high hydrogen pressures have the opposite effect. Here we propose that the  $\text{Ni}_2\text{-OH}$  complex is responsible for the increased mass transport at the surface of the nickel particles relative to that observed in the absence of steam. As discussed below the effect of the  $\text{Ni}_2\text{-OH}$  complex relative to nickel adatoms is to increase the abundance of surface species capable of transporting nickel rather than increasing diffusivity. This hypothesis offers an elegant explanation of the observed changes in the sintering rate upon changes in the partial pressures of steam and hydrogen.

The formation of a  $\text{Ni}_2\text{-OH}$  complex by reaction of one nickel atom placed at a kink and one besides that at a nickel edge site can be written:



As the number of edge and kink atoms are conserved, the energy change associated with this reaction equals a reaction, where a water molecule and two nickel atoms moved from the nickel bulk form a nickel dimer bonded to an OH radical and half a gas-phase hydrogen molecule. We find that a nickel dimer at Ni(111) is stabilized by 87  $\text{kJ mol}^{-1}$  (by attachment of an OH radical) and that the overall energy of formation of a  $\text{Ni}_2\text{-OH}$  complex is endothermic by only 54  $\text{kJ mol}^{-1}$ . The equilibrium constant for formation of a  $\text{Ni}_2\text{-OH}$  complex,  $K_2$ , is given by

$$K_2 = \frac{\theta_{\text{Ni}_2\text{-OH}}}{(1 - 2\theta_{\text{Ni}_2\text{-OH}})^2} \frac{P_{\text{H}_2}^{0.5}}{P_{\text{H}_2\text{O}}}, \quad (4)$$

where  $\theta_{\text{Ni}_2\text{-OH}}$  and  $1 - 2\theta_{\text{Ni}_2\text{-OH}}$  are the coverages of  $\text{Ni}_2\text{-OH}$  species and of free sites at the surface of the nickel particles, respectively. Assuming that  $\theta_{\text{Ni}_2\text{-OH}}$  is small, Eq. (4) may be rewritten:

$$\theta_{\text{Ni}_2\text{-OH}} \approx K_2 \frac{P_{\text{H}_2\text{O}}}{P_{\text{H}_2}^{0.5}}. \quad (5)$$

The results presented above show the energy associated with formation of a  $\text{Ni}_2\text{-OH}$  complex is ca. (112 – 54)  $\text{kJ mol}^{-1}$  = 58  $\text{kJ mol}^{-1}$  lower than that of a nickel adatom. This indicates that in the presence of high pressures of steam and low pressures of hydrogen the abundance of  $\text{Ni}_2\text{-OH}$  species at the surface of the nickel particles will be much higher than that of nickel adatoms. In order to compare the mass transport due to the  $\text{Ni}_2\text{-OH}$  complex with that of the nickel adatom the energies associated with diffusion of a nickel adatom and a  $\text{Ni}_2\text{-OH}$  complex are calculated.

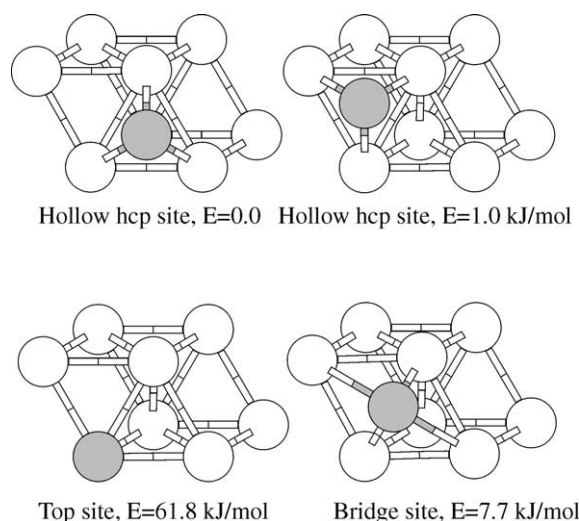


Fig. 2. Adsorption sites, and relative energies, for a Ni adatom on Ni(111). Adatom is shown in gray, substrate atoms in white. Top two layers of the substrate are shown.

The stable and metastable positions of a Ni atom on Ni(111) are shown in Fig. 2. The lowest energy sites are the hollow fcc and hcp sites. The top site is very unfavorable energetically, whereas the bridge site is only  $8 \text{ kJ mol}^{-1}$  higher in energy than the hollow hcp site. Therefore, diffusion of a Ni adatom will happen through bridge sites and not top sites. The diffusion barrier is ca.  $8 \text{ kJ mol}^{-1}$ .

Characteristic geometries for adsorbed  $\text{Ni}_2\text{-OH}$  complex are shown in Fig. 3. The minimum energy structures are those involving both Ni adatoms on fcc hollow sites (configuration (a)) or hcp hollow sites (configuration (b)). The structure with one Ni atom on an fcc hollow site and the other on hcp (configuration (c)) is higher in energy by  $10 \text{ kJ mol}^{-1}$ . When both atoms are on bridge sites (configuration (d)), the energy is  $23 \text{ kJ mol}^{-1}$  higher than the energy of (a).

We performed Nudged Elastic Band (NEB) calculations for several possible diffusion processes of a  $\text{Ni}_2\text{-OH}$  complex to a neighboring site on Ni(111). The energies along the diffusion paths are shown in Fig. 4. We start from the minimum energy configuration, with both Ni adatoms on fcc hollow sites (configuration (a),  $E = 0$ ). We considered five different diffusion possibilities:

- (i) One Ni adatom will remain in the fcc hollow site, while the other passes through the bridge site ( $E = 15 \text{ kJ mol}^{-1}$ ) and ends up on an hcp hollow site (configuration (c),  $E = 10 \text{ kJ mol}^{-1}$ ). After that, the next atom will move to the neighboring bridge site ( $E = 15 \text{ kJ mol}^{-1}$ ), and then descend into the threefold hcp hollow site. Now both Ni adatoms are in hollow hcp sites (configuration (b) rotated,  $E = 3 \text{ kJ mol}^{-1}$ ). The  $\text{Ni}_2\text{-OH}$  complex now moves in the direction of the Ni–Ni bond so that both Ni adatoms are on bridge sites (configuration (d),  $E = 23 \text{ kJ mol}^{-1}$ ). After passing a

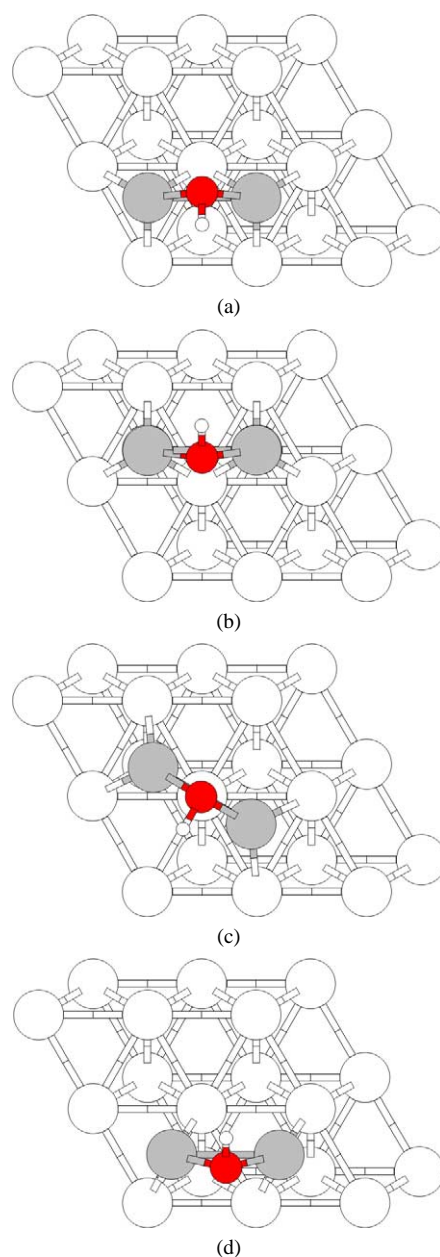


Fig. 3. Stable adsorption sites and relative energies for a  $\text{Ni}_2\text{-OH}$  complex on Ni(111): (a) both Ni atoms on hollow fcc sites,  $E = 0.0$ ; (b) both Ni atoms on hollow hcp sites,  $E = 2.5 \text{ kJ mol}^{-1}$ ; (c) one Ni atom on a hollow fcc site, and the other on a hollow hcp site,  $E = 10.0 \text{ kJ mol}^{-1}$ ; (d) both Ni atoms on bridge sites,  $E = 22.9 \text{ kJ mol}^{-1}$ . Substrate Ni atoms (only top two layers shown) are colored white; adatoms, gray; O, dark gray; H, white.

small energy barrier of  $24 \text{ kJ mol}^{-1}$ , the  $\text{Ni}_2\text{-OH}$  complex ends up having both Ni adatoms in fcc hollow sites (configuration (a) rotated,  $E = 0$ ). The barrier of  $24 \text{ kJ mol}^{-1}$  is due to the necessary switch of the OH group from one side of the Ni–Ni bond to the other. The process described is the minimum energy diffusion path, and is represented by diamonds and a solid line in Fig. 4. The intermediate configurations are also shown in the same figure. The overall diffusion barrier is  $24 \text{ kJ mol}^{-1}$ .

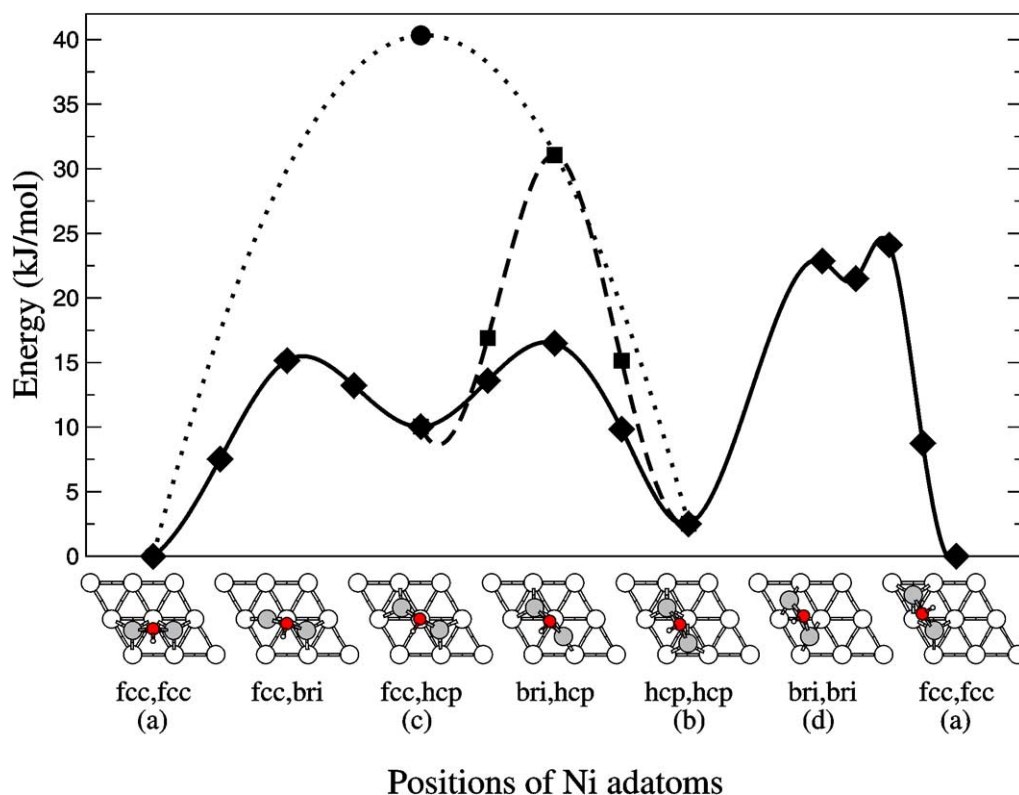


Fig. 4. Energy along the diffusion path for diffusion of  $\text{Ni}_2\text{-OH}$  complex on Ni(111). Top views of snapshots of the diffusion process are shown below. The coloring of atoms is the same as in Fig. 3. The minimum energy path is represented by diamonds and a solid line. A transition between (c) and (b) through a clockwise rotation is shown by squares and a dashed line. The direct translation of the  $\text{Ni}_2\text{-OH}$  complex perpendicular to the Ni–Ni bond is represented by a circle and a dotted line. In all cases, the lines represent cubic spline interpolations between calculated energies.

- (ii) The same process could also happen by simultaneous clockwise rotational motion of the two adatoms, going from configuration (a) to (b) of Fig. 4, without passing through (c). In this case, the transition state will be configuration (d) rotated, so the barrier will be  $23 \text{ kJ mol}^{-1}$ . Then the diffusion from (b) to (a) will be identical as in case (i) described before, resulting again in a barrier of  $24 \text{ kJ mol}^{-1}$ .
- (iii) A third possibility is to go from (a) to (c) as in case (i), but then continue the rotational motion of the  $\text{Ni}_2\text{-OH}$  complex and end up in a configuration identical to (b) of Fig. 3. This transition is represented by squares and a dashed line in Fig. 4. The diffusion from (b) to (a) will involve the same energetics as in case (i). The energy barrier in this case will be  $31 \text{ kJ mol}^{-1}$ .
- (iv) In this case, the  $\text{Ni}_2\text{-OH}$  complex goes from (a) to (b) directly, with both Ni atoms moving at the same time and in the same direction, perpendicular to the Ni–Ni bond. This transition is represented by a circle and a dotted line in Fig. 4. In the transition state, both Ni adatoms are on bridge sites, having a substrate Ni atom under the O atom. The diffusion energy barrier now is much higher, namely  $40 \text{ kJ mol}^{-1}$ . The higher energy barriers associated with the last two processes are due to the fact that in both cases the transition states involve an elongated Ni–Ni bond, as a substrate Ni atom lies between the two Ni adatoms. In addition, the OH group has to be switched from one side of the Ni–Ni bond to the other, which also contributes to the higher transition state energy.
- (v) Finally, the  $\text{Ni}_2\text{-OH}$  complex can move from (a) to a configuration symmetrical to (b) passing through (d) with both Ni atoms moving at the same time and in the same direction, parallel to the Ni–Ni bond. This situation is the opposite to the last part of the process described in (i) (from (b) to (d) and then to (a)). Therefore, the energy barrier would be the same, that is  $24 \text{ kJ mol}^{-1}$ .
- To summarize the previous analysis, we conclude that the minimum energy barrier for diffusion of a  $\text{Ni}_2\text{-OH}$  complex on Ni(111) is  $24 \text{ kJ mol}^{-1}$ . There are two different processes that involve the same transition state: in one (process (i) or (ii)) the  $\text{Ni}_2\text{-OH}$  complex ends up in a rotated configuration; in the other (process (v)) the  $\text{Ni}_2\text{-OH}$  complex has moved in the direction of the Ni–Ni bond. In both cases the transition state is very similar to configuration (d) of Fig. 3, with the difference that the H atom is almost above O. This difference in the position of the H atom accounts for the small difference of about  $1 \text{ kJ mol}^{-1}$  between the transition state and the stable configuration (d).

The barrier for diffusion of a Ni adatom at Ni(111) was only 8 kJ mol<sup>-1</sup>, 16 kJ mol<sup>-1</sup> lower than that of Ni<sub>2</sub>-OH. The reason for the enhancement in the rate of sintering in the presence of steam is that OH-bonded nickel dimers are more abundant than nickel adatoms at the surface of the nickel particles. The effect of the surface concentration of nickel dimers at nickel particles has to be included in the description of the diffusion of nickel particles. Expressions, connecting the surface concentrations and the diffusion constants of OH bonded nickel dimers and nickel adatoms to the diffusion constant of nickel particles, are given in the following section.

## 6. Calculations of the diffusion coefficient for a nickel particle

The objective of this section is to obtain expressions for the diffusion constants of nickel particles when nickel adatoms or Ni<sub>2</sub>-OH complexes are responsible for the mass transport at the surface of the nickel particles and thereby for the rate of sintering.

Gruber [28] derived an expression for the diffusion of gas bubbles in metals, which also describes the diffusion of spherical metallic particles on a planar noninteracting ceramic carrier [29]. The obtained expression links the diffusion constant for metal atoms,  $D_{\text{atom}}$ , at a metal particle to the diffusion of the metal particle,  $D_{\text{particle}}$ ,

$$D_{\text{particle}} = 0.301 D_{\text{atom}} \left( \frac{a_0}{r} \right)^4, \quad (6)$$

where  $a_0$  is the interatomic distance and  $r$  is the particle radius. To derive this expression Gruber [28] used that a flux of metal atoms across a unit length,  $J_s$ , is given by

$$J_s = vV, \quad (7)$$

where  $V$  is the average drift velocity of the atoms and  $v$  is the surface density of the atoms involved in surface diffusion. Gruber [28] determined  $v$  for a (111) facet for a face-centered-cubic lattice to be  $v = a_0^{-2}$  assuming that all atoms in the (111) surface are involved in the diffusion. However, not all the surface atoms in a (111) facet are involved in the mass transport at a given time. The mass transport at the surface of a metal particle takes place via diffusion of adatoms or small nickel islands. The Gibbs free energy of formation of adatoms or small movable islands, which are able to transport mass around the metal particle, determines the concentration of the transporting species. To estimate the concentration of nickel adspecies at the surface, the energies of the adspecies achieved from the DFT calculations are used in the following.

With nickel adatoms as the main transport species at the particle surface,  $v$  is given by

$$v = \theta_{\text{add-atom}} a_0^{-2} \approx K_1 a_0^{-2}, \quad (8)$$

where  $K_1$  is the equilibrium constant for the formation of nickel adatoms at Ni(111) as discussed previously.  $K_1$  determines the concentration of adatoms at the Ni(111) facet.

The equilibrium, which determines the concentration of OH-bonded nickel dimers is approximated by

$$\theta_{\text{Ni}_2\text{-OH}} = K_2 \frac{P_{\text{H}_2\text{O}}}{P_{\text{H}_2}^{0.5}}. \quad (5)$$

Under steam-reforming conditions, the equilibrium among water vapor, hydrogen, and OH-bonded nickel dimers at the nickel surface is most likely established. For example, a total isotopic scrambling in H<sub>2</sub>O/D<sub>2</sub> mixtures is obtained at a temperature of 200 °C while a temperature of 450 °C is necessary before total isotopic scrambling is obtained in CD<sub>4</sub>/H<sub>2</sub> mixtures [30]. In addition, the lowest barrier for dehydrogenation of methane over nickel is calculated to be 39 kJ mol<sup>-1</sup> higher than for the lowest barrier for abstraction of a hydrogen atom from a water molecule [23].

From Eq. (5),  $v$  is calculated to be

$$v = 2\theta_{\text{Ni}_2\text{-OH}} a_0^{-2} \approx 2K_2 a_0^{-2} \frac{P_{\text{H}_2\text{O}}}{P_{\text{H}_2}^{0.5}}. \quad (9)$$

Following Gruber [28] and using the expressions derived for  $v$  above, the diffusion constant for a moving spherical nickel particle on a plane noninteracting support can be derived. In the case where adatoms are responsible for the mass transport the diffusion constant may be expressed:

$$D_{\text{particle}}^{\text{add-atom}} = 0.301 D_{\text{add-atom}} \left( \frac{a_0}{r} \right)^4 K_1. \quad (10)$$

When OH-bonded nickel dimers dominate nickel surface transport then the diffusion coefficient for the nickel particles is given by

$$D_{\text{particle}}^{\text{OH-dimer}} = 0.602 D_{\text{OH-dimer}} \left( \frac{a_0}{r} \right)^4 K_2 \frac{P_{\text{H}_2\text{O}}}{P_{\text{H}_2}^{0.5}}. \quad (11)$$

The DFT calculations show that the energy involved in forming an adatom is 112 kJ mol<sup>-1</sup> while the energy involved in forming a nickel dimer bonded to an OH radical is only 54 kJ mol<sup>-1</sup>. However, the activation energy of diffusion is 16 kJ mol<sup>-1</sup> lower for nickel adatoms than for Ni<sub>2</sub>-OH complexes at Ni(111).

In the following the relative rates of diffusion of nickel particles due to Ni<sub>2</sub>-OH and Ni adatoms at  $P_{\text{H}_2\text{O}}/P_{\text{H}_2}^{0.5} = 1$  and  $T = 500$  °C will be estimated. The entropy difference involved in the mass transport using adatoms and Ni<sub>2</sub>-OH complexes will be neglected. Furthermore, the difference in the activation energy of diffusion between the two species of 16 kJ mol<sup>-1</sup> determined by DFT calculations will be used. Using these assumptions and using the energy of formation calculated above the rate of the mass transport due to Ni<sub>2</sub>-OH is determined to be approximately 700 times higher than that due to nickel adatoms. Hence, the rate of sintering will be dominated by the Ni<sub>2</sub>-OH species.

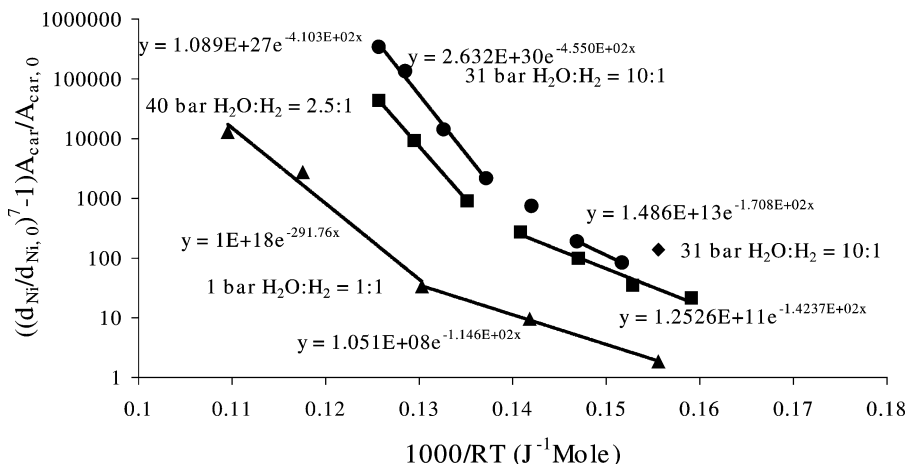


Fig. 5.  $((\bar{d}_{\text{Ni}}/\bar{d}_{\text{Ni},0})^7 - 1)(A_{\text{car}}/A_{\text{car},0})$  for samples of catalyst No. 1 (22 wt% Ni/MgAl<sub>2</sub>O<sub>4</sub>) and catalyst No. 2 (9.5 wt% Ni/Al<sub>2</sub>O<sub>3</sub>) plotted as a function of  $1000/RT$ . Catalyst No. 1 was sintered for 700 h in an atmosphere with a steam to hydrogen ratio of 2.5:1 and 40 bar total pressure (filled squares, this work) or with a steam to hydrogen ratio of 10:1 and 31 bar total pressure (filled circles, [9]). Catalyst No. 2 was sintered for 50 h in an atmosphere with a steam to hydrogen ratio of 10:1 and 1 bar total pressure (filled triangles) or a steam to hydrogen ratio of 10:1 and 31 bar total pressure (filled diamond). The lines are fits of Arrhenius type expressions to the experimental data. See text for details.

## 7. Sintering of nickel catalysts

With the expressions for  $D_{\text{particle}}^{\text{add-atom}}$  and  $D_{\text{particle}}^{\text{OH-dimer}}$ , the energies obtained by DFT calculations, and the expression for the time development during sintering of the average nickel particle diameter [9], it is possible to rationalize the experimental data quantitatively. The expression for the time-dependent average nickel particle diameter,  $\bar{d}_{\text{Ni}}$ , using  $D_{\text{particle}} = D_{\text{particle}}^{\text{add-atom}}$  is given by

$$\bar{d}_{\text{Ni}} = \left( \text{const} \frac{K_1 D_{\text{add-atom}} X_{\text{Ni}} \tau}{(1 - X_{\text{Ni}}) A_{\text{car}}} + \bar{d}_{\text{Ni},0}^7 \right)^{1/7}, \quad (12)$$

where  $X_{\text{Ni}}$  is the weight fraction of nickel,  $A_{\text{car}}$  is the surface area of the carrier per gram of carrier,  $\tau$  is the sintering time,  $\bar{d}_{\text{Ni},0}$  is the average nickel particle diameter of the fresh sample,  $K_1$  is defined by Eq. (2), and “const” is an arbitrary constant.

As noted previously, the observed rate of sintering depends on  $P_{\text{H}_2\text{O}}$  and  $P_{\text{H}_2}$ , suggesting that Ni<sub>2</sub>-OH complexes dominate the rate of sintering. This hypothesis is also supported by the DFT calculations presented above. The experimental data are therefore interpreted using  $D_{\text{particle}} = D_{\text{particle}}^{\text{OH-dimer}}$ . The time-dependent average nickel particle diameter,  $\bar{d}_{\text{Ni}}$ , is then given by

$$\bar{d}_{\text{Ni}} = \left( \text{const} \frac{K_2 D_{\text{OH-dimer}} X_{\text{Ni}} \tau}{(1 - X_{\text{Ni}}) A_{\text{car}}} \left( \frac{P_{\text{H}_2\text{O}}}{P_{\text{H}_2}^{0.5}} \right) + \bar{d}_{\text{Ni},0}^7 \right)^{1/7}. \quad (13)$$

By rewriting this equation and defining the sintering constant,  $x_{\text{particle-migration}} = (\bar{d}_{\text{Ni}}/\bar{d}_{\text{Ni},0})^7 - 1$ , the slope of a plot of the logarithm of this quantity against  $1000/RT$  equals the energy of formation of the Ni<sub>2</sub>-OH complex,  $E_2$ , plus the activation energy for its diffusion at the nickel surface,

$E_{\text{diffusion, Ni}_2\text{-OH}}$ :

$$\begin{aligned} \ln(x_{\text{particle-migration}}) &= \ln \left( \left( \frac{\bar{d}_{\text{Ni}}}{\bar{d}_{\text{Ni},0}} \right)^7 - 1 \right) \\ &= \ln \left( \text{const} \frac{A_2 A_{\text{OH-dimer}} X_{\text{Ni}} \tau}{(1 - X_{\text{Ni}}) A_{\text{car}} \bar{d}_{\text{Ni},0}^7} \left( \frac{P_{\text{H}_2\text{O}}}{P_{\text{H}_2}^{0.5}} \right) \right) \\ &\quad - \frac{E_2 + E_{\text{diffusion, Ni}_2\text{-OH}}}{RT}. \end{aligned} \quad (14)$$

It should be noted here that Eqs. (12)–(14) are only true when the sintering proceeds via particle migration and coalescence. This point is important as Ostwald ripening may dominate sintering at higher temperatures as discussed below.

In Fig. 5, the logarithm of

$$x_{\text{particle-migration}} \frac{A_{\text{car}}}{A_{\text{car},0}} = \left( \left( \frac{\bar{d}_{\text{Ni}}}{\bar{d}_{\text{Ni},0}} \right)^7 - 1 \right) \frac{A_{\text{car}}}{A_{\text{car},0}}$$

is plotted as a function of  $1000/RT$  for experimental series 1 and 2 and for the data reported in Ref. [9].  $A_{\text{car}}/A_{\text{car},0}$  is the ratio of the surface area per gram of carrier of the sintered and the fresh catalyst, respectively. The reason for this correction factor is that  $A_{\text{car}}$  decreases during sintering. According to Eq. (14),  $x_{\text{particle-migration}}$  increases with decreasing carrier surface area. When correcting  $x_{\text{particle-migration}}$  with  $A_{\text{car}}/A_{\text{car},0}$ ,  $A_{\text{car}}$  measured at the end of the sintering experiment is used in Eq. (14). This modification is not accurate but only an approximate correction. However,  $A_{\text{car}}/A_{\text{car},0}$  is a relative moderate correction factor and furthermore, the carrier surface area decreases fast in the beginning and then reaches an almost stable level after a period of sintering as observed for catalyst No. 2 [11]. Therefore, the carrier surface area is close to the end value during most of the sintering time.

The total surface areas (BET) of the catalysts were measured for all samples of catalyst No. 2; Assuming in accordance with the results in Ref. [8] that nickel particles add approximately the same total surface area as it occupies, correcting the data for catalyst No. 2 is easy. However, for catalyst No. 1, the BET areas were only determined for catalyst samples sintered at the highest and the lowest temperatures. The BET areas were 65 and 86% of that of the fresh sample, respectively. This loss of surface area may be caused by loss of carrier surface area as well as nickel surface area. It is assumed here in accordance with Refs. [8,9] that the loss in BET area is due to a decrease in the surface area of the carrier and that the BET areas of the catalyst samples at intermediate temperatures can be determined by interpolation using the following expression,  $A_{\text{BET}}(T) = A_{\text{BET}}^{\infty} e^{-E_a/RT}$ . The correction factor,  $A_{\text{car}}/A_{\text{car},0}$ , gives rise to a correction of less than 8% in the activation energies of the data in Fig. 5.

Several interesting conclusions may be drawn from Fig. 5. First, sintering at the same pressure of steam but at elevated hydrogen pressure decreases the rate of sintering as also concluded from Fig. 1. This observation can now be rationalized by Eq. (14). The  $P_{\text{H}_2\text{O}}/P_{\text{H}_2}^{0.5}$  ratio in Eq. (14) predicts a decrease in  $x_{\text{particle-migration}}$  for catalyst No. 1 of a factor of 2 for the experimental conditions used here compared to those employed by Sehested [9]. A factor of 1.7 is obtained at low temperatures in good agreement with the theoretical considerations, but at higher temperatures the factor is approximately 6 (see Fig. 5, filled squares and filled circles). The latter observation is discussed below.

A second interesting feature of the three sets of data plotted in Fig. 5 is that they all apparently show both a low and a high temperature sintering regime with two different activation energies of sintering. The two data sets obtained using catalyst No. 1 show a change in the activation energy in the temperature range  $T_{\text{change}} = 546\text{--}604^\circ\text{C}$ . However, the sintering data from sintering series No. 2 show that the activation energy for sintering of catalyst No. 2 at ambient pressure does not change until temperatures reaches the range  $650\text{--}750^\circ\text{C}$ . The high and low temperature activation energies determined from the straight lines in Fig. 2 are the following: Series 1, 142 and  $410\text{ kJ mol}^{-1}$  in the temperature intervals  $483\text{--}581$  and  $617\text{--}684^\circ\text{C}$ , respectively; Ref. [9], 171 and  $455\text{ kJ mol}^{-1}$  in the temperature intervals  $520\text{--}546$  and  $604\text{--}684^\circ\text{C}$ , respectively; Series 2, 115 and  $292\text{ kJ mol}^{-1}$  in the temperature intervals  $500\text{--}650$  and  $650\text{--}825^\circ\text{C}$ , respectively.

There are considerable differences between these activation energies and prefactors even within the low and the high temperature regimes, respectively. However, from the data in Fig. 5 it seems reasonable to conclude that the activation energies for the high pressure experiments are similar. However, the activation energies of the low pressure experiments seem to fall below those derived by the high pressure experiments. The reason for this apparent discrepancy is discussed below.

In Fig. 5, considerable changes in the activation energies are seen at approximately  $600^\circ\text{C}$  for the high pressure data and at higher temperature for the low pressure data. One explanation for the increase in activation energy is that a change in the sintering mechanism takes place. As discussed previously, particle migration and coalescence is believed to be the dominating sintering mechanism at low temperatures [9,31]. The evidence for the latter conclusion was discussed in more detail by Sehested [9] and may be summarized as follows: (i) The nickel particle-size distributions after sintering at moderate temperatures are log normal [3,5,6,8,11] and these types of distributions result from particle migration and coalescence [29,31–34]. (ii) The parameter  $n$  in Eq. (15) is generally 7 or higher for  $T < 700^\circ\text{C}$  [7,35]

$$-\frac{dA_{\text{Ni}}}{dt} = kA_{\text{Ni}}^n, \quad (15)$$

where  $A_{\text{Ni}}$  is the nickel surface area as a function of the time and  $k$  is a rate constant for sintering. (iii) A higher activation barrier for sintering is expected for Ostwald ripening than for particle migration and coalescence [9,35].

Interestingly, a temperature of ca.  $700^\circ\text{C}$  seems to be the threshold of the literature data, where Ostwald ripening is believed to gain importance [7,9,11,35]. This is in agreement with the temperature for the observed change in the activation energy for the low pressure data in Fig. 5. Rasmussen et al. [11] determined  $n$  in Eq. (15) to be 8 by fitting this equation to the time dependence of the nickel surface area of catalyst No. 2 after sintering at  $650^\circ\text{C}$ ,  $\text{H}_2\text{O}:\text{H}_2 = 1:1$ , and 1 bar total pressure. This observation indicates [29,35] that at this temperature the sintering mechanism is particle migration and coalescence. In Fig. 5, the observed change in the activation energy for the sintering process takes place at relative low temperatures ( $546\text{--}617^\circ\text{C}$ ) when the sintering experiment is conducted at high pressures (high pressures of steam) and hence more severe conditions. This could be interpreted as the change in mechanism take place at lower temperatures when more severe sintering conditions (high pressures of steam) are used. Altogether, the change of the sintering mechanism from particle migration and coalescence to Ostwald ripening (atomic migration) offers a possible explanation of both the observations reported in the literature and the data plotted in Fig. 5. However, due to the lack of more solid evidence for this interpretation of the data, Ostwald ripening is not discussed further and the focus in the discussions below is sintering at low temperatures.

It is interesting to compare the experimentally observed activation energies at low temperature to that expected by theoretical considerations. The expected activation energy for sintering via particle migration can be estimated from the sum of the energies of formation of the  $\text{Ni}_2\text{--OH}$  complex of  $54\text{ kJ mol}^{-1}$  and the energy of diffusion of this species over a  $\text{Ni}(111)$  of  $24\text{ kJ mol}^{-1}$ . Hence, the activation energy of sintering via particle migration and coalescence is estimated to be  $78\text{ kJ mol}^{-1}$ . The presence of adsorbed H atoms on the surface will increase the activation energy by twice the adsorption energy of an H atom times the coverage of H. As the

adsorption energy of H on Ni(111) is  $43 \text{ kJ mol}^{-1}$  [2], the increase in the activation energy can be estimated to lie in the range of  $60\text{--}85 \text{ kJ mol}^{-1}$  for the high pressure experiments. For the low pressure experiments, the increase in the activation energy will lie in the range of  $25\text{--}75 \text{ kJ mol}^{-1}$ . This can possibly account for the change in the measured activation energy between the high and low pressure experiments. Adding this correction to the calculated activation energy of  $78 \text{ kJ mol}^{-1}$ , we find a very good agreement with the measured values of 115, 142, and  $171 \text{ kJ mol}^{-1}$ .

As a test of Eq. (14) it is interesting to compare the sintering results obtained for catalyst No. 2 at low and at high pressure at  $500^\circ\text{C}$ . This can be done because both sets of data are expected to sinter via particle migration and coalescence at  $500^\circ\text{C}$ . For this sintering mechanism Eq. (14) can be used to calculate the effect of sintering time and partial pressures of steam and hydrogen. The rate of sintering is much higher at 31 bar total pressure than at 1 bar total pressure. The increase in the sintering constant,  $x_{\text{particle-migration}}$ , upon changing the atmosphere over catalyst No. 2 from 1 bar total pressure and  $\text{H}_2\text{O}:\text{H}_2 = 1:1$  to 30 bar total pressure and  $\text{H}_2\text{O}:\text{H}_2 = 10:1$  at  $500^\circ\text{C}$  is calculated to be

$$\begin{aligned} \frac{D_{\text{particle}}^{30 \text{ bar, H}_2\text{O}:\text{H}_2=10:1}}{D_{\text{particle}}^{1 \text{ bar, H}_2\text{O}:\text{H}_2=1:1}} &= \frac{P_{\text{H}_2\text{O}}^{30 \text{ bar, H}_2\text{O}:\text{H}_2=10:1} (P_{\text{H}_2}^{1 \text{ bar, H}_2\text{O}:\text{H}_2=1:1})^{0.5}}{P_{\text{H}_2\text{O}}^{1 \text{ bar, H}_2\text{O}:\text{H}_2=1:1} (P_{\text{H}_2}^{30 \text{ bar, H}_2\text{O}:\text{H}_2=10:1})^{0.5}} \\ &= \frac{28.18 \times 0.5^{0.5}}{0.5 \times 2.82^{0.5}} \approx 23.7. \end{aligned} \quad (16)$$

To calculate the total increase in the sintering constant,  $x_{\text{particle-migration}}$ , the sintering time of 115 h at high pressure and 50 h at low pressure should be taken into account. It is calculated that the sintering constant increases by a factor of 55 upon changing the sintering conditions from 1 bar total pressure and  $\text{H}_2\text{O}:\text{H}_2 = 1:1$  for 50 h to 31 bar total pressure and  $\text{H}_2\text{O}:\text{H}_2 = 10:1$  for 115 h. Experimentally, the value of  $x_{\text{particle-migration}}$  is increased by a factor of 75. This agreement is reasonable considering the simplicity of the model and the huge change in conditions.

It is also of interest to compare the rate of sintering of catalysts No. 1 and No. 2 at  $500^\circ\text{C}$ , 31 bar and  $\text{H}_2\text{O}:\text{H}_2 = 10:1$ . The sintering constant,  $x_{\text{particle-migration}}$ , is given by

$$x_{\text{particle-migration}} = \text{const} \frac{K_2 D_{\text{OH-dimer}} X_{\text{Ni}} \tau}{(1 - X_{\text{Ni}}) A_{\text{car}} d_{\text{Ni},0}^7} \left( \frac{P_{\text{H}_2\text{O}}}{P_{\text{H}_2}^{0.5}} \right). \quad (17)$$

The parameters used to calculate the ratio of the sintering constants for catalysts No. 2 and No. 1 assuming similar values of “const” are  $\tau_1 = 700 \text{ h}$ ,  $\tau_2 = 115 \text{ h}$ ,  $X_{\text{Ni}}$  (catalyst No. 1) = 0.22,  $X_{\text{Ni}}$  (catalyst No. 2) = 0.095,  $d_{\text{Ni},0,1}/d_{\text{Ni},0,2} = 2.18$ , and  $A_{\text{car},1}/A_{\text{car},2} = 1/6$ . Using these ratios, the ratio of  $x_{\text{particle-migration}}$  (catalyst No. 2)/ $x_{\text{particle-migration}}$  (catalyst No. 1) is calculated to be 2.4. The value obtained by comparing the high pressure data point

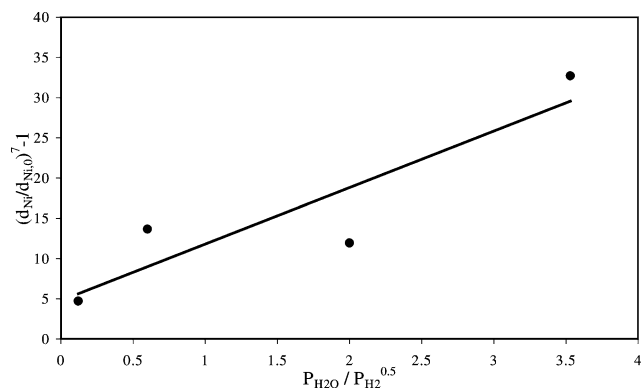


Fig. 6.  $((\bar{d}_{\text{Ni}}/\bar{d}_{\text{Ni},0})^7 - 1)$  for catalyst samples with 19.4 wt% nickel supported on an  $\text{Al}_2\text{O}_3$  carrier (catalyst No. 3) plotted as a function of  $P_{\text{H}_2\text{O}}/P_{\text{H}_2}^{0.5}$ . The catalyst was sintered for 50 h at  $550^\circ\text{C}$  and 1 bar total pressure with the steam to hydrogen ratio varied by two orders of magnitude. The line is a linear least-squares fit to the data. See text for details.

for catalyst No. 2 to an extrapolation between the two nearest data points for catalyst No. 1 is 3.2. The similarity in “const” for the two types of supports may be ascribed to the similarity in the wetting angle between metal particles and ceramic carriers for most systems [36].

The data for catalysts No. 1 and No. 2 and the way they fit with the theoretical considerations give confidence in the model used here to explain the data. Further support for the model proposed here can be found in Fig. 6 where the data from Table 3 are plotted. In this figure,  $x_{\text{particle-migration}} = (\bar{d}_{\text{Ni}}/\bar{d}_{\text{Ni},0})^7 - 1$  for catalyst No. 3 obtained after sintering at a total pressure of 1 bar and  $550^\circ\text{C}$  for 50 h is plotted as a function of  $P_{\text{H}_2\text{O}}/P_{\text{H}_2}^{0.5}$ . Under these conditions, particle migration and coalescence are expected to be the prevailing sintering mechanism due to the low pressure and relative low temperature.  $x_{\text{particle-migration}}$  is according to Eq. (17) expected to be proportional to  $P_{\text{H}_2\text{O}}/P_{\text{H}_2}^{0.5}$  and within the uncertainty this is also what is observed from Fig. 6. Hence, the data in Fig. 6 further support the conclusion that the  $\text{Ni}_2\text{--OH}$  dimer is the transport species for nickel at the surface of nickel particles in the presence of steam and hydrogen.

The model used above gives a good quantitative description of the observed data at low temperatures. It seems reasonable to assume that steam influences the rate of sintering by increasing the concentration of nickel dimers at the surface of the nickel particles. According to this model, there will be a threshold value of the  $P_{\text{H}_2\text{O}}/P_{\text{H}_2}^{0.5}$  ratio where mass transport at the nickel particles due to OH-bonded nickel dimers and free nickel adatoms will be equally important. It is also interesting to note that the highest values of the  $P_{\text{H}_2\text{O}}/P_{\text{H}_2}^{0.5}$  ratio are found at the entrance of a prereformer or a fired reformer; hence this factor speeds up the sintering at the entrance of the reforming unit. Sintering is also more severe at the outer shell of a catalyst in the case where the effectiveness factor for a catalyzed reaction is less than one, which is normally the case for reforming.

## 8. Conclusions

This paper provides new insight into the mechanism of sintering of supported nickel catalysts and supported metal catalysts in general. Especially, the influences of the partial pressures of steam and hydrogen on the rate of sintering have been addressed in this paper using experimental data and DFT calculations. The increased rate of sintering in the presence of steam is attributed to formation of Ni<sub>2</sub>–OH species at the surface of nickel particles. The energy of formation of this species at the nickel surface is low compared to that of nickel adatoms while the energy of diffusion is highest for the Ni<sub>2</sub>–OH complex. It is concluded from the DFT calculations that in the presence of steam and hydrogen the surface transport at nickel particles will be dominated by Ni<sub>2</sub>–OH dimers. The calculated energies of formation and diffusion are used in a simple model that is able to predict the rate of sintering of nickel catalysts. The predicted dependencies of temperature,  $P_{\text{H}_2\text{O}}$ , and  $P_{\text{H}_2}$  are in good agreement with those obtained experimentally.

The experimental data show a change in the activation energy of sintering at high temperatures. The temperature for this change is at approximately 600 °C at 40 bar total pressure and H<sub>2</sub>O:H<sub>2</sub> = 2.5:1 when the catalyst is sintering for 700 h. At ambient pressure, the change is observed to happen at approximately 700 °C after sintering at 1 bar total pressure and H<sub>2</sub>O:H<sub>2</sub> = 1:1 for 50 h. It is speculated that the rate of sintering at high temperatures may be determined by Ostwald ripening.

In conclusion, the formulas in this paper provide a tool for predicting sintering data and hence the performance of industrial reformers assuming that Ni<sub>2</sub>–OH is dominating sintering under these conditions. Furthermore, the new insight into the mechanism of sintering may eventually result in new and better catalysts.

## Acknowledgments

We thank Ulla Ebert, Erik Christensen, Henning Kosack, and Jakob Skibsted Jensen for technical assistance and Joachim Jacobsen for discussions of the manuscript.

## References

- [1] J.R. Rostrup-Nielsen, in: J.R. Anderson, M. Boudart (Eds.), *Catalysis, Science and Technology*, vol. 5, Springer, Berlin, 1984, Chap. 1.
- [2] J.R. Rostrup-Nielsen, J. Sehested, J.K. Nørskov, *Adv. Catal.* 47 (2002) 65.
- [3] J.T. Richardson, J.G. Crump, *J. Catal.* 57 (1979) 417.
- [4] A. Teixeira, R. Giudici, *Chem. Eng. Sci.* 54 (1999) 3609.
- [5] H.K. Kuo, P. Ganesan, R.J. Deangelis, *J. Catal.* 64 (1980) 303.
- [6] C.H. Bartholomew, W.L. Sorensen, *J. Catal.* 81 (1983) 131.
- [7] C.H. Bartholomew, *Appl. Catal. A* 107 (1993) 1.
- [8] J. Sehested, A. Carlson, T.V.W. Janssens, P.L. Hansen, A.K. Datye, *J. Catal.* 197 (2001) 200.
- [9] J. Sehested, *J. Catal.* 217 (2003) 417.
- [10] J.T. Richardson, J.L. Propp, *J. Catal.* 98 (1986) 457.
- [11] F.B. Rasmussen, J. Sehested, H.T. Teunissen, A.M. Molenbroek, B.S. Clausen, *Appl. Catal.* (2004), in press.
- [12] C.H. Bartholomew, R.B. Pannel, R.W. Fowler, *J. Catal.* 79 (1983) 83.
- [13] E. Ruckenstein, B. Pulvermacher, *J. Catal.* 37 (1975) 416.
- [14] T.-M. Ahn, J.K. Tien, P. Wynblatt, *J. Catal.* 66 (1980) 335.
- [15] E. Stassinou, H.H. Lee, *Chem. Eng. Sci.* 50 (1995) 1337.
- [16] C.T. Campbell, S.C. Parker, D.E. Starr, *Science* 298 (2002) 811.
- [17] ASTM D4567, Standard Test Method for Single-Point Determination of Specific Surface Area of Catalysts Using Nitrogen Adsorption by Continuous Flow Method.
- [18] I. Alstrup, J.R. Rostrup-Nielsen, S. Røen, *Appl. Catal.* 1 (1981) 303.
- [19] The DACAPO plane wave/pseudopotential DFT code is available as Open Source Software at <http://www.fysik.dtu.dk/CAMPOS/>.
- [20] D. Vanderbilt, *Phys. Rev. B* 41 (1990) 7892.
- [21] B. Hammer, L.B. Hansen, J.K. Nørskov, *Phys. Rev. B* 59 (1998) 7413.
- [22] M.C. Payne, M.P. Teter, D.C. Allan, T.A. Arias, J.D. Joannopoulos, *Rev. Mod. Phys.* 64 (1992) 1045.
- [23] H.S. Bengaard, J.K. Nørskov, J. Sehested, B.S. Clausen, L.P. Nielsen, A. Molenbroek, J.R. Rostrup-Nielsen, *J. Catal.* 209 (2002) 365.
- [24] D.J. Chadi, M.L. Cohen, *Phys. Rev. B* 8 (1973) 5747.
- [25] H. Jónsson, G. Mills, G.K. Schenter, *Surf. Sci.* 324 (1995) 305.
- [26] S. Hørch, H.T. Lorensen, S. Helveg, E. Lægsgaard, I. Stensgaard, K.W. Jacobsen, J.K. Nørskov, F. Besenbacher, *Nature* 398 (1999) 134.
- [27] P.J. Feibelman, *Phys. Rev. Lett.* 85 (2000) 606.
- [28] E.E. Gruber, *J. Appl. Phys.* 38 (1967) 243.
- [29] P. Wynblatt, N.A. Gjostein, *Prog. Solid State Chem.* 9 (1975) 21.
- [30] L.M. Aparicio, *J. Catal.* 165 (1997) 262.
- [31] C.G. Granqvist, R.A. Buhrman, *Appl. Phys. Lett.* 27 (1975) 693.
- [32] C.G. Granqvist, R.A. Buhrman, *J. Catal.* 46 (1977) 238.
- [33] C.G. Granqvist, R.A. Buhrman, *J. Catal.* 42 (1976) 477.
- [34] C.G. Granqvist, R.A. Buhrman, *J. Appl. Phys.* 47 (1976) 2200.
- [35] R. Hughes, *Deactivation of Catalysts*, Academic Press, London, 1984.
- [36] M. Humenik, W.D. Kingery, *J. Am. Ceram. Soc.* 37 (1954) 18.